AGU PUBLICATIONS

Geochemistry, Geophysics, Geosystems

RESEARCH ARTICLE
10.1002/2016GC006700

Variations in pockmark composition at the Vestnesa Ridge: Insights from marine controlled source electromagnetic and seismic data

Bedanta K. Goswami[1], Karen A. Weitemeyer[1,2], Stefan Bünz[3], Timothy A. Minshull[1], Graham K. Westbrook[1,4,5], Stephan Ker[5], and Martin C. Sinha[1]

[1]National Oceanography Centre Southampton, Ocean and Earth Science, University of Southampton, European Way, Southampton, UK, [2]National Oceanography Centre Southampton, European Way, Southampton, UK, [3]CAGE, UiT Arctic University of Norway, Tromsø, Norway, [4]School of Geography, Earth and Environmental Sciences, University of Birmingham, Birmingham, UK, [5]Geosciences Marines, Ifremer Centre de Brest, Plouzané, France

Key Points:
- Joint analysis of coincident CSEM, 2-D and 3-D seismic reflection data at Vestnesa Ridge
- Strong correlation between high-resistivity anomaly, amplitude blanking, and chaotic seismic reflection patterns
- High levels of free gas and hydrate likely within active chimneys

Correspondence to:
B. K. Goswami,
Bedanta.Goswami@noc.soton.ac.uk

Citation:
Goswami, B. K., K. A. Weitemeyer, S. Bünz, T. A. Minshull, G. K. Westbrook, S. Ker, and M. C. Sinha (2017), Variations in pockmark composition at the Vestnesa Ridge: Insights from marine controlled source electromagnetic and seismic data, *Geochem. Geophys. Geosyst.*, *18*, 1111–1125, doi:10.1002/2016GC006700.

Received 28 OCT 2016
Accepted 3 FEB 2017
Accepted article online 10 FEB 2017
Published online 24 MAR 2017

Abstract The Vestnesa Ridge marks the northern boundary of a known submarine gas hydrate province in the west Svalbard margin. Several seafloor pockmarks at the eastern segment of the ridge are sites of active methane venting. Until recently, seismic reflection data were the main tool for imaging beneath the ridge. Coincident controlled source electromagnetic (CSEM), high-resolution two-dimensional (2-D) airgun, sweep frequency SYSIF, and three-dimensional (3-D) p-cable seismic reflection data were acquired at the south-eastern part of the ridge between 2011 and 2013. The CSEM and seismic data contain profiles across and along the ridge, passing several active and inactive pockmarks. Joint interpretation of resistivity models obtained from CSEM and seismic reflection data provides new information regarding the fluid composition beneath the pockmarks. There is considerable variation in transverse resistance and seismic reflection characteristics of the gas hydrate stability zone (GHSZ) between the ridge flanks and chimneys beneath pockmarks. Layered seismic reflectors on the flanks are associated with around 300 Ωm^2 transverse resistance, whereas the seismic reflectors within the chimneys exhibit amplitude blanking and chaotic patterns. The transverse resistance of the GHSZ within the chimneys vary between 400 and 1200 Ωm^2. Variance attributes obtained from the 3-D p-cable data also highlight faults and chimneys, which coincide with the resistivity anomalies. Based on the joint data interpretation, widespread gas hydrate presence is likely at the ridge, with both hydrates and free gas contained within the faults and chimneys. However, at the active chimneys the effect of gas likely dominates the resistive anomalies.

Plain Language Summary Active methane venting was observed at several seafloor locations at the south-eastern segment of the Vestnesa Ridge in the west Svalbard margin. New geophysical data acquired in the area between 2011 and 2013 provide new constraints at understanding potential factors enabling the active venting in the area. High levels of free gas is inferred beneath the locations of known vents based on the joint analysis of multiple geophysical datasets.

1. Introduction

The Vestnesa Ridge, on the west Svalbard continental margin (Figure 1a) is a deep water gas hydrate system (1200–1350 m water depth) that contains numerous seafloor pockmarks [*Vogt et al.*, 1994; *Bünz et al.*, 2012]. Pockmarks are seafloor depressions [*Hovland et al.*, 2002] that are observed in many hydrate provinces [*Vogt et al.*, 1994; *Hovland et al.*, 2005; *Gay et al.*, 2006; *Westbrook et al.*, 2009; *Sultan et al.*, 2010] and may suggest an active gas release system. Only the pockmarks in the eastern segment of the 100 km long ridge are currently reported to be active, while several inactive pockmarks are present on the western segment [*Petersen et al.*, 2010; *Bünz et al.*, 2012; *Smith et al.*, 2014a]. Variation in the tectonic stresses between the two segments is thought to be a contributing factor toward the differences in pockmark activity between the two segments [*Plaza-Faverola et al.*, 2015].

The presence of hydrates at the Vestnesa Ridge is known on the basis of bottom simulating reflectors (BSRs) observed in seismic reflection data [*Eiken and Hinz*, 1993; *Vogt et al.*, 1994; *Hustoft et al.*, 2009; *Petersen et al.*, 2010; *Bünz et al.*, 2012; *Plaza-Faverola et al.*, 2015]. High amplitude reflections beneath the BSRs indicate

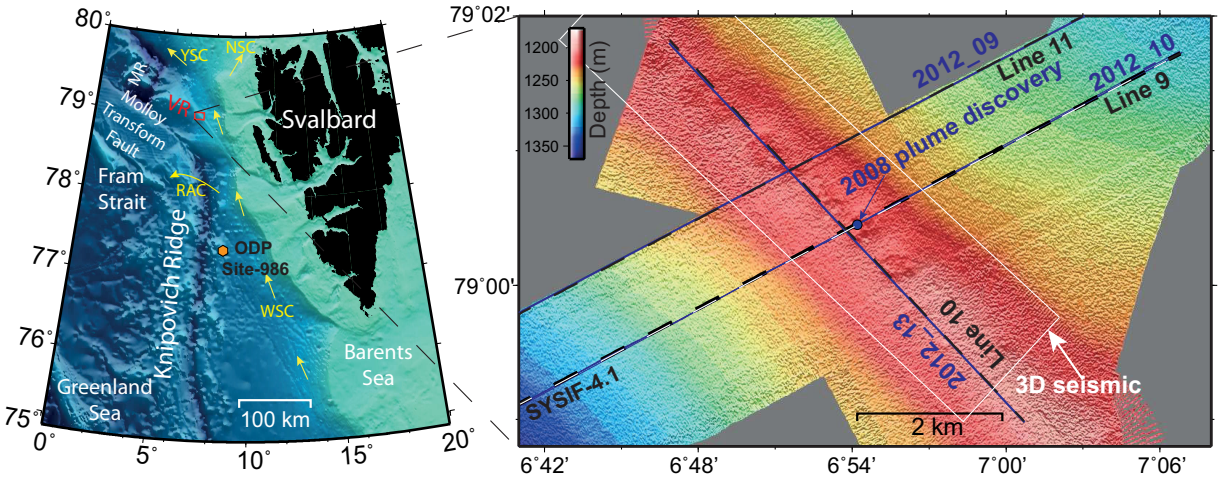

Figure 1. (a) Map of west Svalbard highlighting the Vestnesa Ridge survey area on the regional bathymetry map from international bathymetric chart of the Arctic Ocean (IBCAO) data set [*Jakobsson et al.*, 2012]. VR—Vestnesa Ridge. Ocean currents: WSC—West Spitsbergen Current, NSC—North Spitsbergen Current, YSC—Yermak Slope Current and RAC—Return Atlantic Current. ODP Site 986 (orange dot) provides reference resistivity and porosity. (b) Location of coincident CSEM (dotted black line), high-resolution airgun 2-D seismic reflection survey lines (purple lines), 3-D p-cable seismic survey area (white box) and high-resolution SYSIF seismic reflection survey lines (dashed white line) with multibeam bathymetry data.

the presence of free gas [*Hustoft et al.*, 2009; *Petersen et al.*, 2010; *Bünz et al.*, 2012; *Plaza-Faverola et al.*, 2015]. The observed free gas zone beneath the ridge crest is likely to be over-pressured [*Hustoft et al.*, 2009; *Goswami et al.*, 2015], which may drive fluids toward the seafloor. The over-pressured free gas zone and tectonic stresses are the most likely enabling factors for gas escape through pockmarks that have been observed by several scientific cruises (Figure 2) in the region [*Bünz et al.*, 2012; *Smith et al.*, 2014b]. Acoustic chimneys beneath the pockmarks are widespread at the ridge [*Petersen et al.*, 2010; *Bünz et al.*, 2012; *Smith et al.*, 2014a; *Plaza-Faverola et al.*, 2015] and are the likely pathways for the escaping gas. The seismic reflection characteristics within these chimneys vary widely and to date are the main constraint used to understand variations in fluid composition beneath the pockmarks [*Bünz et al.*, 2012; *Plaza-Faverola et al.*, 2015].

Resistivity obtained from marine controlled source electromagnetic (CSEM) data is highly sensitive to both hydrate and free gas within sediments. It is often used in drilling to detect hydrate and gas since they are more resistive than saline pore waters [*Collett and Ladd*, 2000]. Both hydrate and free gas are expected to be present in chimneys within the GHSZ [*Liu and Flemings*, 2007; *Bünz et al.*, 2012; *Goswami et al.*, 2015]. Therefore, CSEM data provide a good complement to seismic data in order to better understand differences between pockmarks. In this paper, (1) resistivity models obtained from CSEM data at the south-eastern segment of the Vestnesa Ridge are presented, which provide volume information on the presence of gas and/or hydrate saturations; and (2) these models are used with coincident seismic reflection data to infer differences in pore fluid composition beneath the pockmarks.

2. Geological Summary

The Vestnesa Ridge (Figure 1a) is a 100 km long, boomerang-shaped feature. It sits on top of a relatively young oceanic crust (<20 Ma), near the ultraslow spreading Molloy Ridge and the Knipovich Ridge, in the west Svalbard continental margin. The ridge is formed of 2–5 km thick sediments that have been influenced by seafloor spreading, ocean currents and glaciation [*Eiken and Hinz*, 1993; *Forsberg et al.*, 1999]. The sediments are primarily contourites and their thickness increases toward the east [*Eiken and Hinz*, 1993; *Hustoft et al.*, 2009]. The geological setting of the ridge makes it conducive to the presence of gas and hydrates within the shallow sediments [*Eiken and Hinz*, 1993].

3. Data Summary

Data from four different geophysical sources are presented in this paper. The primary focus of the paper is the CSEM data, which were acquired in 2012. Three CSEM lines were acquired at the south-eastern segment

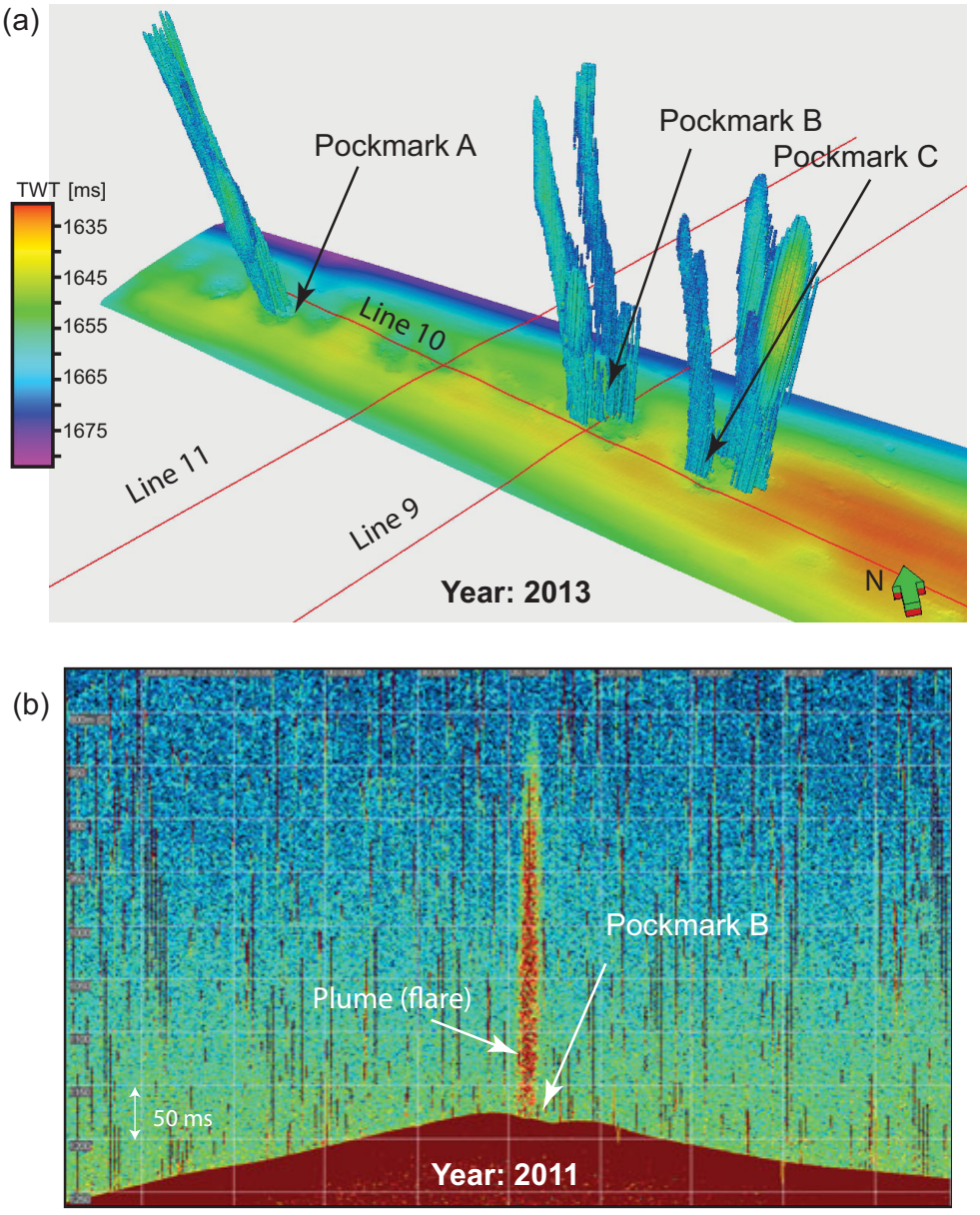

Figure 2. (a) Position of acoustic flares seen in the water column on single-beam EK60 echosounder data [*Smith et al*., 2014a] is superimposed above seafloor pockmarks at the south-eastern part of the Vestnesa Ridge. The seafloor bathymetry is extracted from the 3-D p-cable seismic data acquired in 2013. The flares were found to be active during repeated surveys in 2010, 2012, 2013, and 2015. (b) Position of an active plume on Pockmark B, acoustically imaged with the EK60 data in 2011.

of the Vestnesa Ridge using a towed triaxial electric-field receiver—Vulcan [*Constable et al*., 2016] and CSEM transmitter—DASI [*Sinha et al*., 1990] (Figure 1b). Line 9 and Line 11 were acquired in a roughly south-west to north-easterly direction (~75°) perpendicular to the ridge axis, whereas Line 10 was acquired along the ridge in a south-east to north-westerly (~319°) direction. Line 9 passes over the top of a pockmark that was active during previous geophysical cruises between 2008 and 2011. Line 10 was designed to pass over several pockmarks along the ridge, some of which were active during previous cruises, while Line 11 passes across a pockmark that is not known to be active (Figure 1b). DASI was towed ~50 m above the seafloor and transmitted a 1 Hz square waveform of ~81 A current across its 100 m long horizontal electric dipole antenna. Vulcan recorded the transmitted signal across its 2 m long inline dipole antenna and 1 m long cross-line and vertical dipole antennae, 300 m behind the tail of the DASI antenna. Further details of methods used to process the Vulcan data can be found in *Goswami et al*. [2016].

Coincident two-dimensional (2-D) high-resolution airgun seismic reflection data were also acquired during this survey (Figure 1b). Details of acquisition and processing of the 2-D seismic reflection data can be found in *Goswami et al*. [2015]. This paper also presented a resistivity model obtained from inversion of nine ocean bottom electric-field receivers and a Vulcan pseudosection for Line 9.

High-resolution seismic data using a deep-towed seismic system called SYSIF [*Marsset et al*., 2010] were acquired in the study area in 2011 (Figure 1b). SYSIF was towed at an altitude of 100 m above the seafloor and provides a higher resolution subsurface image compared to the airgun data due to its higher frequency [*Ker et al*., 2014]. One of the SYSIF lines coincident with CSEM Line 9 is used here for interpretation. These data have a frequency bandwidth of 220–1050 Hz that provides a vertical resolution of 1 m [*Ker et al*., 2010].

The high-resolution three-dimensional (3-D) seismic data presented in this paper were acquired in 2013 using the p-cable system [*Planke et al*., 2009]. The p-cable system consisted of 14 parallel streamers each 25 m long. A mini-GI gun with chamber volumes of 15/15 in^3 was used as a source and shot every 6 s, providing a bandwidth of 30–400 Hz. Further details on the acquisition and processing parameters are given by *Plaza-Faverola et al*. [2015]. The 3-D seismic data have a spatial sampling of 6.25 m. 3-D seismic interpretation was done in Schlumberger's Petrel package and included horizon interpretation and attribute mapping. The variance attribute volume of the 3-D seismic data is identical to that of *Plaza-Faverola et al*. [2015]. The variance attribute provides a measurement of dip and azimuth variability of adjacent seismic traces along major reflections [*Plaza-Faverola et al*., 2015].

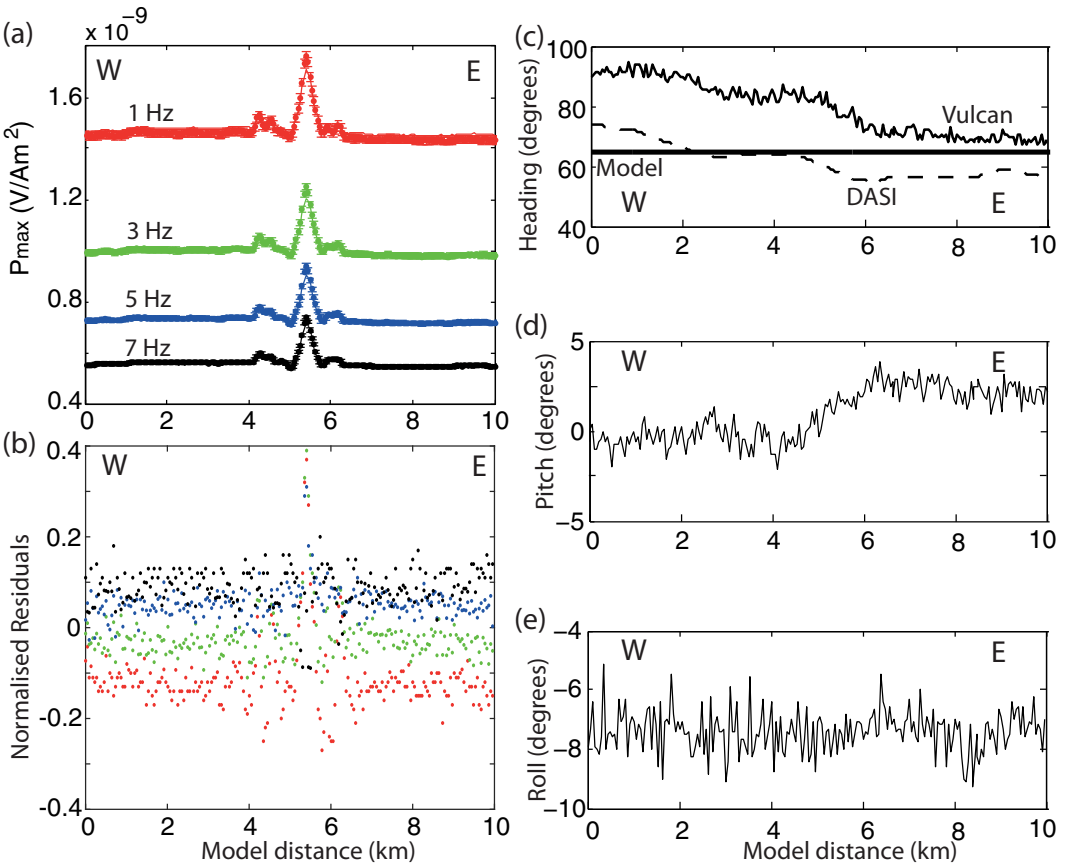

Figure 3. (a) A good model to data fit is observed for all frequencies (1 Hz (red), 3 Hz (green), 5 Hz (blue), 7 Hz (black)) for Line 9; (b) residuals normalized by data error are small for all frequencies. The small amount of frequency bias of residuals is likely due to the unknown dip of the antenna. (c) The model axis (thick solid line) is assumed along the average heading (measured clockwise from geographical North) of the DASI (dashed line). Vulcan heading (solid line), (d) pitch and (e) roll data are recorded by a compass and tilt-meter mounted on Vulcan and was used to rotate Vulcan data into model axis before computing P_{max}.

Hydroacoustic water column data acquired in 2011 and 2013 [*Smith et al*., 2014a] are shown in Figure 2. No hydroacoustic data were acquired along with the CSEM survey, as it interferes with the underwater navigation system used for positioning DASI.

4. Resistivity Models

The 2-D inversion code MARE2DEM [*Key and Ovall*, 2011; *Key*, 2016] is used to invert the Vulcan data. This involves a 2.5-D finite element forward code [*Key and Ovall*, 2011] and a regularized nonlinear Occam's inversion [*Constable et al*., 1987] to output a smooth resistivity model. Our analysis uses the magnitude of the major axis of the polarization ellipse (P_{max}) [*Smith and Ward*, 1974] traced by the horizontal electric-field vectors, as recorded by Vulcan for the fundamental transmission frequency (1 Hz) and the first three harmonics (3, 5, and 7 Hz). The P_{max} data show significant variation in the value of P_{max} across the three profiles at the Vestnesa Ridge (Figures 3a, 4a, and 5a), which hints toward considerable lateral heterogeneity in shallow subsurface resistivity. The heading, pitch, and roll of Vulcan recorded during the survey are used for the P_{max} calculations (plots c–e of Figures 3–5).

Based on the variance computed during processing of the Vulcan data, a 0.1% error in P_{max} and a target misfit of 1 was specified for the inversions. The starting model for the inversion consists of a highly resistive air layer (10^{12} Ωm), seawater with 10 horizontal layers of constant resistivity based on data obtained from a conductivity, temperature, depth (CTD) probe, and a sediment resistivity of 1 Ωm beneath the seafloor. Only the sediment resistivity was a free parameter in the inversion. The inversion mesh consists of triangular elements that are finer at the seabed (minimum 30 m edge length) and coarser beyond the profile edges and at depth. A horizontal smoothing factor of 3 times vertical smoothing is specified. Isotropic as well as

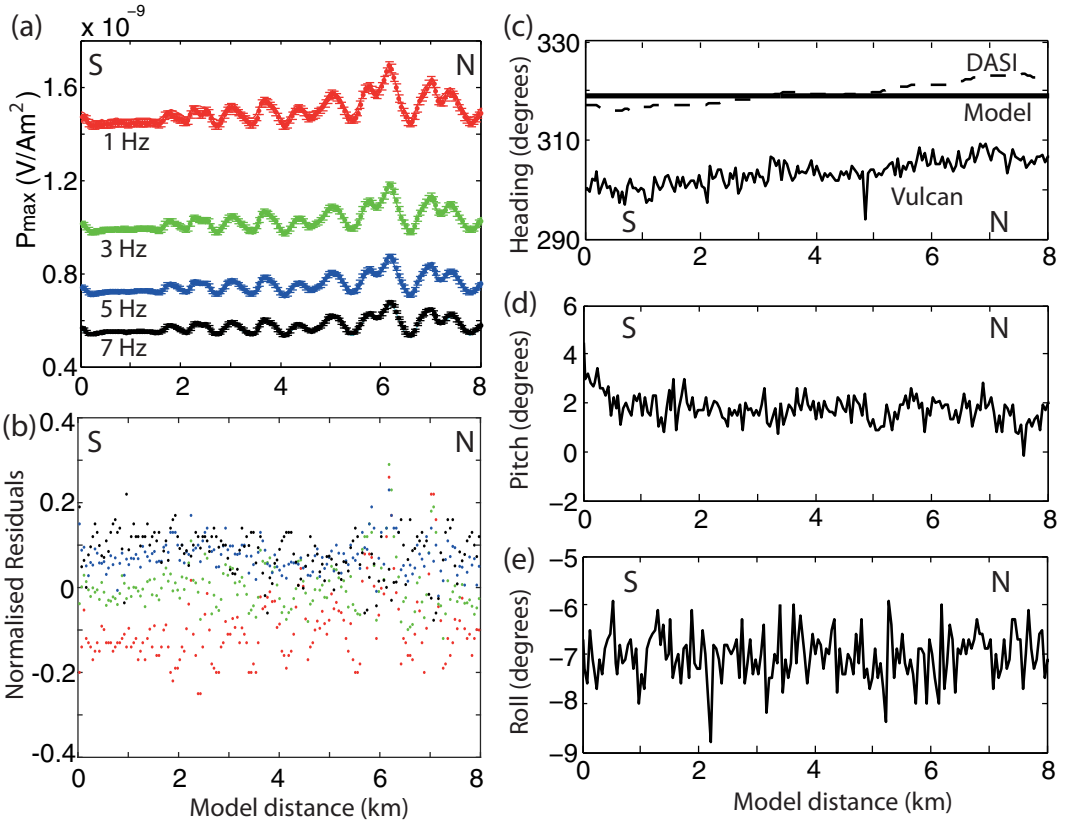

Figure 4. (a) Heterogeneity in P_{max} values can be observed at all frequencies used in the inversion for Line 10. A good model to data fit is observed for all frequencies (1 Hz (red), 3 Hz (green), 5 Hz (blue), 7 Hz (black)) and (b) residuals normalized by data error are small for all frequencies. (c) The model axis (thick solid line) is assumed along the average heading (measured clockwise from geographical North) of the DASI (dashed line). Vulcan heading (solid line), (d) pitch and (e) roll data are recorded by a compass and tilt-meter mounted on Vulcan and was used to rotate Vulcan data into model axis before computing P_{max}.

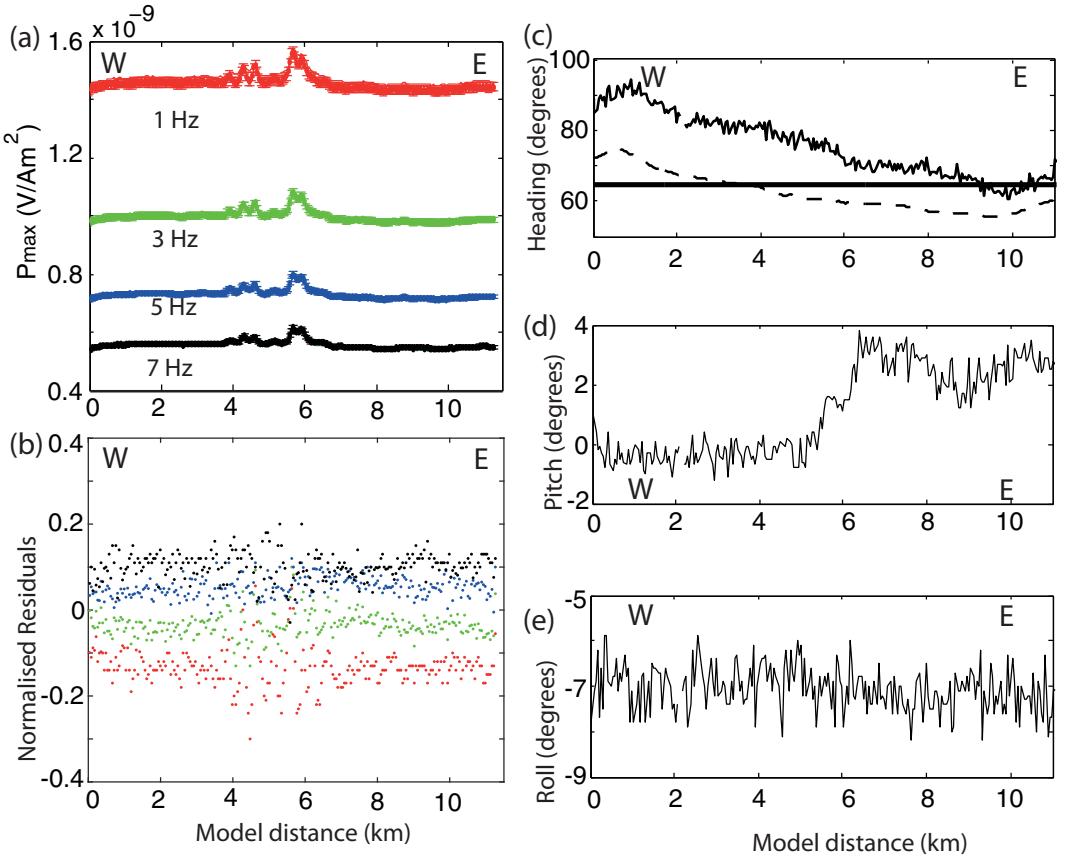

Figure 5. (a) A good model to data fit is observed for all frequencies (1 Hz (red), 3 Hz (green), 5 Hz (blue), 7 Hz (black)) and (b) residuals normalized by data error are small for all frequencies on Line 11. The small amount of frequency bias of residuals is likely due to the unknown dip of the antenna. (c) The model axis (thick solid line) is assumed along the average heading (measured clockwise from geographical North) of the DASI (dashed line). Vulcan heading (solid line), (d) pitch and (e) roll data are recorded by a compass and tilt-meter mounted on Vulcan and was used to rotate Vulcan data into model axis before computing P_{max}.

vertical transverse-isotropic (VTI) inversions produced very similar resistivity models. Only the vertical resistivity models from the anisotropic (VTI) inversion are discussed in this paper because (i) VTI anisotropy is a good assumption for layered marine sediments and (ii) the horizontal resistivity models are not well constrained, as no cross-line data were used in the VTI inversions [*MacGregor and Tomlinson*, 2014; *Ramananjaona et al*., 2011]. Further analysis of the Vulcan inversion method can be found in *Goswami et al*. [2016]. The Occam inversions shown here output the smoothest model that fits the data within the specified misfit tolerance, for given data error [*Key*, 2012b; *Constable et al*., 1987].

The resistivity models in Figures 6a, 7a, and 8a, obtained from the inversions show significant lateral changes in resistivity both along and across the Vestnesa Ridge. A good fit of model to data is observed for the three lines, for the given target misfit and data errors (Figures 3a, 3b, 4a, 4b, 5a, and 5b). The sensitivity contours provide a measure of how changes in various parts of the model affect the model response. Lower sensitivity parts of the model are therefore associated with higher resistivity uncertainty. In addition, since the CSEM method used is more sensitive to the transverse resistance (resistivity times thickness, Figures 6b, 7b, and 8b) than the resistivity [*Constable*, 2010], the Vulcan models sometime slightly overestimate the very shallow resistivity and underestimate the resistivity at low sensitivities. This was also noticed in synthetic model studies of Vulcan data [*Goswami et al*., 2016].

For the lines across the ridge, the western flanks show 2–2.5 Ωm resistivity whereas the eastern flanks show around 3–3.5 Ωm resistivity (Figures 6a and 8a). High-resistivity pockets beneath the ridge axis are observed on both Line 9 and Line 11. On Line 9 (Figure 6), the high-resistivity pocket is observed as a 4–30 Ωm high-resistivity chimney that is 500 m wide (between 5.3 and 5.8 km model distance), whereas on Line 11

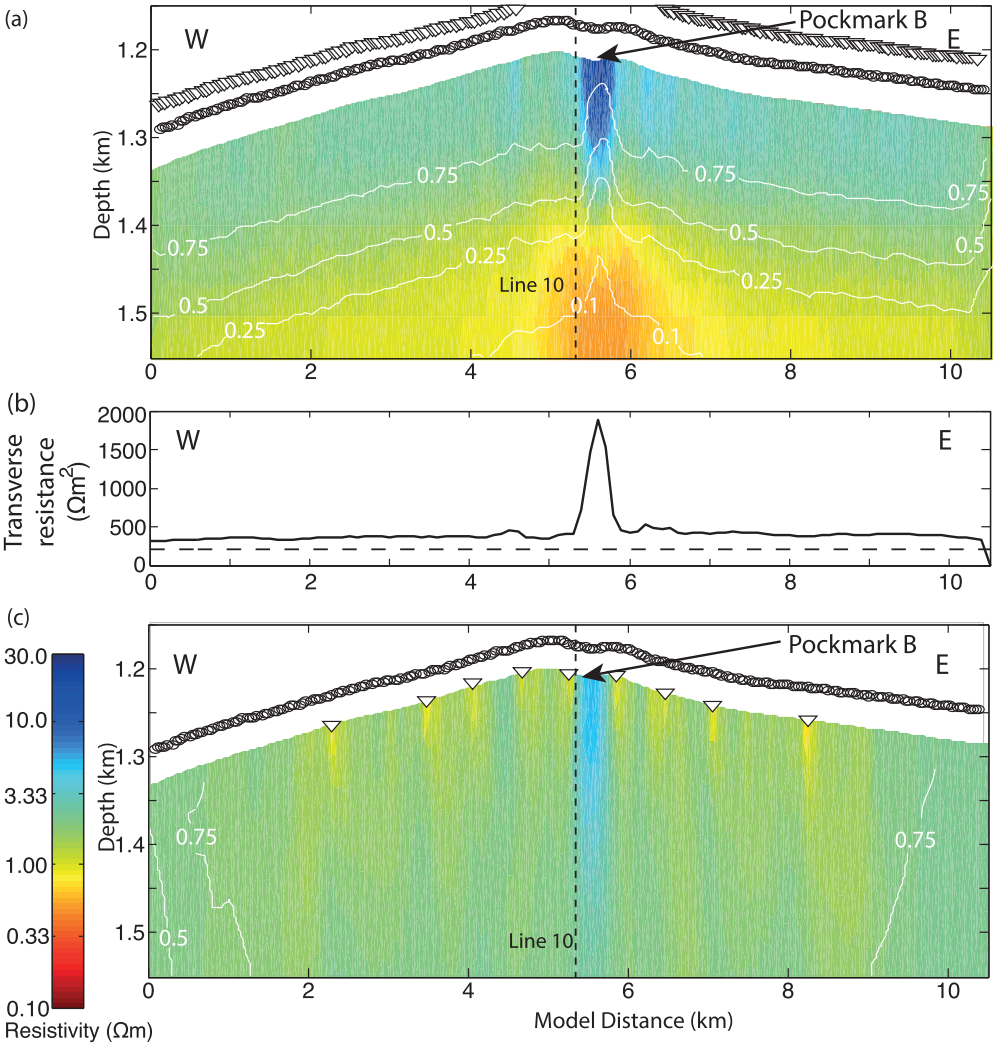

Figure 6. (a) Resistivity model obtained from VTI inversion of Vulcan P_{max} data on Line 9. Position of DASI is shown in circles and position of Vulcan is shown as inverted triangles. Pockmark B was active during geophysical cruises between 2008 and 2011. (b) Transverse resistance for the top 180 mbsf for the resistivity model (solid line) and reference transverse resistance (dashed line) from ODP Site 986. A target misfit of 1 was used for the inversion. (c) Resistivity model obtained from VTI inversion of ocean bottom electric-field (OBE) receivers adapted from *Goswami et al.* [2015]. Position of DASI is shown in circles and position of OBEs is shown as inverted triangles. The OBE resistivity model is shown in the model coordinates of the Vulcan model. Contour overlay (thin white lines) shows data sensitivity to model features (0.5 = 50% sensitivity) in plots a and c. The conductive pocket below 25% sensitivity in the Vulcan model is likely to be a model artifacts.

(Figure 8), the high-resistivity pocket is around 200 m wide and has a maximum resistivity of 8 Ωm. In addition, ∼100 m wide, vertical high-resistivity zones of 4–5 Ωm resistivity are also observed at 4.5, 6.2, and 6.5 km model distance on Line 9 (Figure 6). Evidence of narrow vertical resistive zones similar to those on Line 9 is also observed on Line 11, but is less pronounced (Figure 8).

On Line 10, which runs along the top of the ridge, eight pockets of high resistivity are observed (Figure 7a). Most of these high-resistivity zones toward the southern part of the line have 3.5–5 Ωm resistivity and are around 100–150 m wide. The resistivity anomaly at 4 km model distance, where Line 9 intersects Line 10 has a resistivity of 4–8 Ωm and is around 400 m wide directly beneath the seafloor. The anomaly between 5 and 5.5 km model distance has a resistivity of 5–6 Ωm and is located at the intersection between Line 10 and Line 11. The high-resistivity pockets on the northern part of the line are around 800 m wide and show resistivities of 4–15 Ωm. Outside these pockets, the resistivity within the shallow sediments along the ridge is around 2.5–3 Ωm.

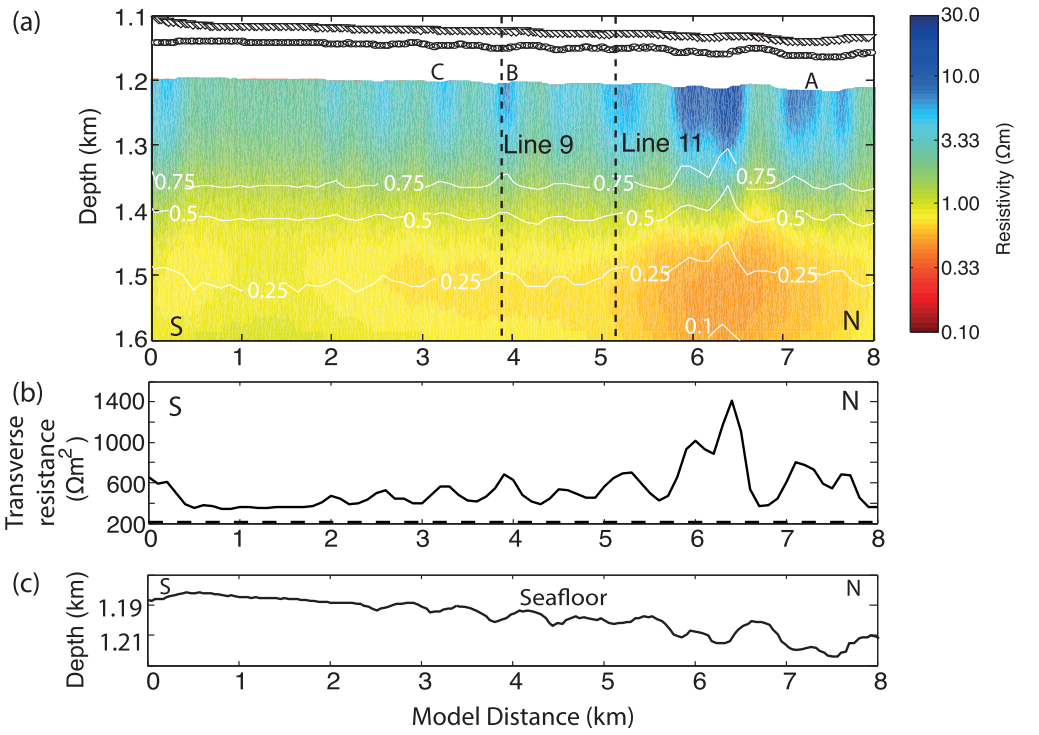

Figure 7. (a) Resistivity model obtained from VTI inversion of Vulcan P_{max}. Position of DASI is shown in circles and position of Vulcan is shown as inverted triangles. Pockmarks A, B, and C were active during previous geophysical cruises. Contour overlay (thin white line) shows data sensitivity to model features (0.5 = 50% sensitivity). The conductive pockets below 25% sensitivity in the model, beneath the highly resistive chimneys are likely to be a model artefact.(b) Transverse resistance for the top 180 mbsf for the resistivity model (solid line) and reference transverse resistance (dashed line) from ODP Site 986. (c) The seafloor profile shows the undulating bathymetry for Line 10 containing seafloor pockmarks. A target misfit of 1 was used for the inversion.

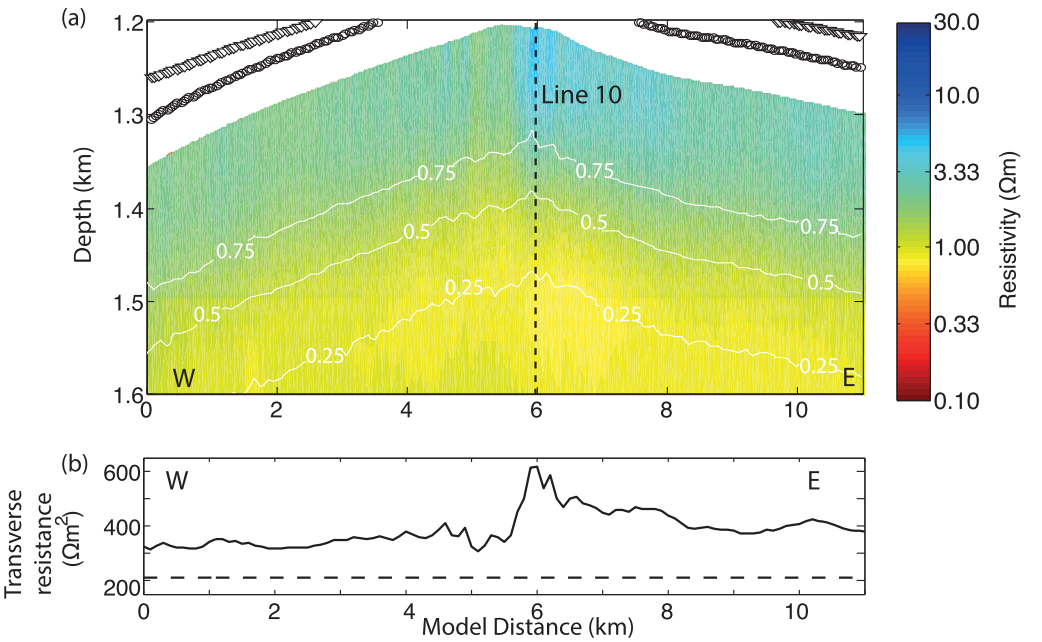

Figure 8. (a) Resistivity model obtained from VTI inversion of Vulcan P_{max} data on Line 11. Position of DASI is shown in circles and position of Vulcan is shown as inverted triangles. Contour overlay (thin white line) shows data sensitivity to model features (0.5 = 50% sensitivity). (b) Transverse resistance for the top 180 mbsf for the resistivity model (solid line) and reference transverse resistance (dashed line) from ODP Site 986. A target misfit of 1 was used for the inversion.

5. Discussion

The CSEM and seismic data sets sampled several pockmarks at the Vestnesa Ridge that are known to have varying activity of gas seeps. Three of the pockmarks along the crest of the ridge (A, B, and C, Figure 2a) show acoustic gas flares in the water column indicating active seepage of gas. These gas flares have been observed to be active in 2010, 2012 [*Smith et al*., 2014a], 2013, and 2015, and the pockmark B at the intersection of Line 9 and Line 10 was also active in 2008 (Figure 2b). Line 10 along the crest lies at the margin of the two active pockmarks in the SE (B and C), crosses three inactive pockmarks and runs along the NW margin of another active pockmark (A). Line 9 directly crosses an active pockmark whereas Line 11 crosses an inactive pockmark. It should be noted that potentially all pockmarks are active and that in addition to the free gas flux into the water column, there might also be a diffusive flux as dissolved phase. However,

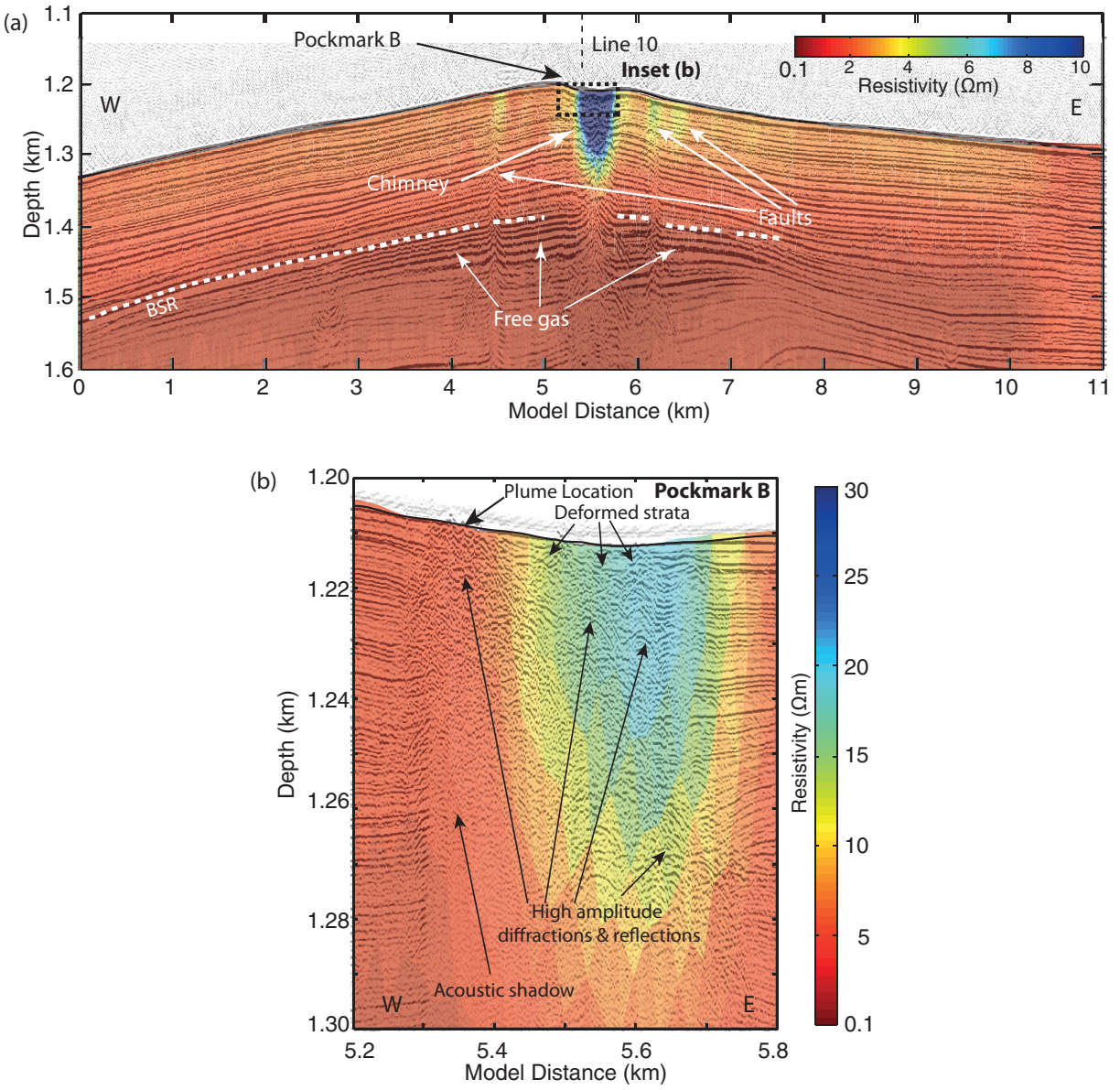

Figure 9. (a) Overlay of vertical resistivity model for Line 9 and coincident airgun seismic reflection data 2012–10 shows good agreement between areas of elevated resistivity and acoustic chimneys. Note the change in color scale for resistivity from Figure 6. The resistivity model has negligible sensitivity to the free gas beneath the BSR. (b) Overlay of vertical resistivity model for Line 9 and coincident SYSIF-4.1 seismic reflection data for the central chimney shows asymmetry in the distribution of high-amplitude reflections, highest resistivity, and acoustic shadow. Note the change in resistivity scale used for inset (b) to illustrate the high-resistivity values within the central chimney.

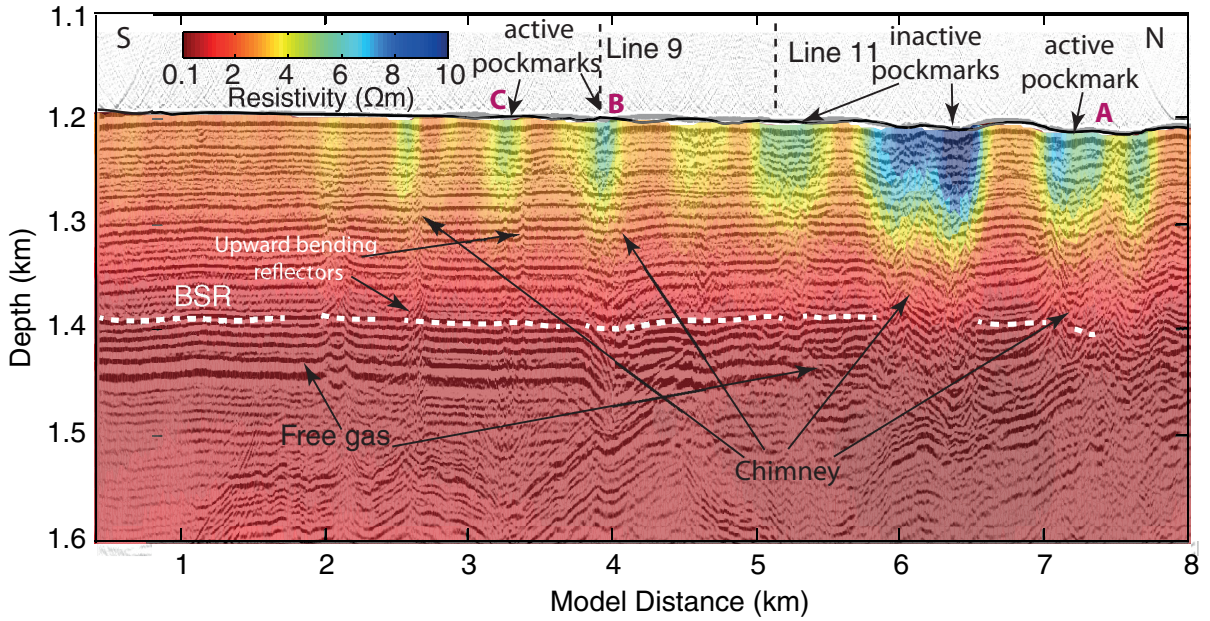

Figure 10. Overlay of vertical resistivity model for Line 10 and coincident airgun seismic reflection data 2012-13 shows good agreement between areas of elevated resistivity and acoustic chimneys. Note the change in color scale for resistivity from Figure 7. The reflectors associated with free gas has very low sensitivity in the resistivity models.

the free gas flux indicates that the three active pockmarks (A, B, and C) have noticeable elevated methane gas concentrations compared to the inactive ones [*Hong et al*., 2016].

A good lateral correlation between the elevated resistivities, pockmarks, location of acoustic chimneys, and variance attributes can be found in coincident CSEM and seismic data (Figures 9–11). Resistivity variations can be caused by changes in porosity, pore fluid saturation, pore fluid salinity, temperature, mineralogy, and grain fabric of the host sediments [*Ellis et al*., 2010]. On the basis of the geological history of the Vestnesa Ridge and the similarity of seismic reflection characteristics across the ridge [*Eiken and Hinz*, 1993; *Hustoft et al*., 2009; *Bünz et al*., 2012; *Plaza-Faverola et al*., 2015], the mineralogy and grain fabric of the host sediments in the study area are likely to be laterally uniform. Bottom water temperatures (50 m above the seafloor) were recorded using a CTD probe mounted on DASI. These data show uniform temperatures along and across the ridge. For the short distances of our CSEM profiles, the geothermal gradients are assumed to be similar. Therefore, background pore water salinity and resistivity is assumed to vary with depth but not

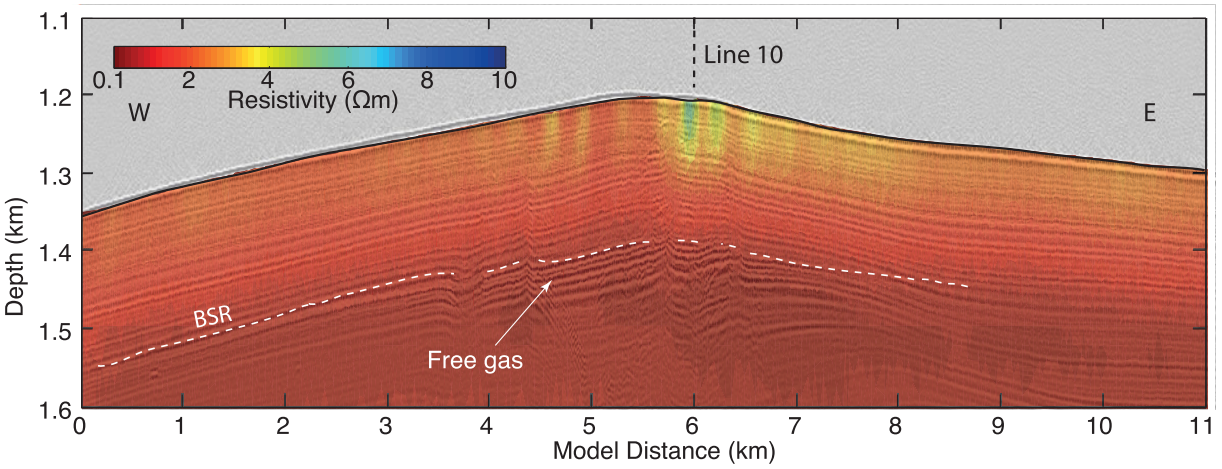

Figure 11. Overlay of vertical resistivity model for Line 11 and coincident seismic reflection data 2012-09 shows good agreement between areas of elevated resistivity and acoustic chimneys. Note the change in color scale for resistivity from Figure 8. The resistivity model has extremely small sensitivity to the free gas.

laterally. Since the ridge consists largely of hemipelagic sediments [*Eiken and Hinz*, 1993; *Howe et al*., 2008], the nearby ODP Site 986 [*Jansen et al*., 1996] with similar sediments and water depth is used as a reference for estimating the background resistivity trend. These data suggest around 1–1.2 Ωm resistivity for the water saturated hemipelagic sediments. The presence of more resistive material (e.g., hydrate or gas) is therefore, the most likely cause of the elevated resistivities in the resistivity models. Elevated resistivities and reflection push downs [*Bünz et al*., 2012] provide strong arguments for the presence of free gas, while elevated resistivities and reflection pull ups [*Plaza-Faverola et al*., 2010] support presence of hydrate within such features.

The different data sets presented here were not acquired simultaneously and therefore not perfectly coincident. However, since the resistivity models obtained from the CSEM data are governed by diffusive electromagnetic energy propagation, the small errors in position are considered acceptable for the joint interpretation of the resistivity models and the different seismic data sets. The resistivity models obtained from Vulcan data are likely to have sensitivity to the top 250 mbsf [*Goswami et al*., 2016], but the sensitivity decreases with depth. The BSR observed in the study area is at approximately 180 mbsf [*Bünz et al*., 2012; *Hustoft et al*., 2009; *Plaza-Faverola et al*., 2015]. However, we do not expect a resistivity anomaly associated with the BSR due to low free gas saturations (2–5%, *Hustoff et al*. [2009]; *Goswami et al*. [2015]) beneath the GHSZ and diffusive energy propagation for the CSEM method. Beneath the BSR, the model sensitivities decrease rapidly and they approach the starting resistivity of 1 Ωm (Figures 6a, 7a, and 8a). The low model sensitivities lead to higher uncertainty in the resistivity models beneath the BSR, where gas saturations are expected to be low. We, therefore, limit the joint interpretation of resistivity and seismic data to the GHSZ only. The seismic data provides information about the free gas zone (FGZ) beneath the BSR.

5.1. Chimneys

Several chimney structures have been identified within the GHSZ based on the resistivity, 2-D/3-D seismic data (Figures 9–11) and attributes derived from the seismic data [*Bünz et al*., 2012; *Plaza-Faverola et al*., 2015; *Smith et al*., 2014b]. The variance time slice [*Plaza-Faverola et al*., 2015] extracted ∼50 m beneath the seafloor from 3-D p-cable seismic data shows the chimneys as incoherent, chaotic, and almost circular structures with clearly defined extents (Figure 12). These chimneys are the likely pathways for gas migration from the over-pressured FGZ to the pockmarks [*Hustoft et al*., 2009; *Bünz et al*., 2012]. High-amplitude reflections related to the FGZ are limited only to the western flank and beneath the ridge crest (Figures 9a and 11). This asymmetry is likely due to the lateral migration of gas beneath the GHSZ, from the ultraslow spreading ridge to the west of the study area [*Bünz et al*., 2012; *Hustoft et al*., 2009].

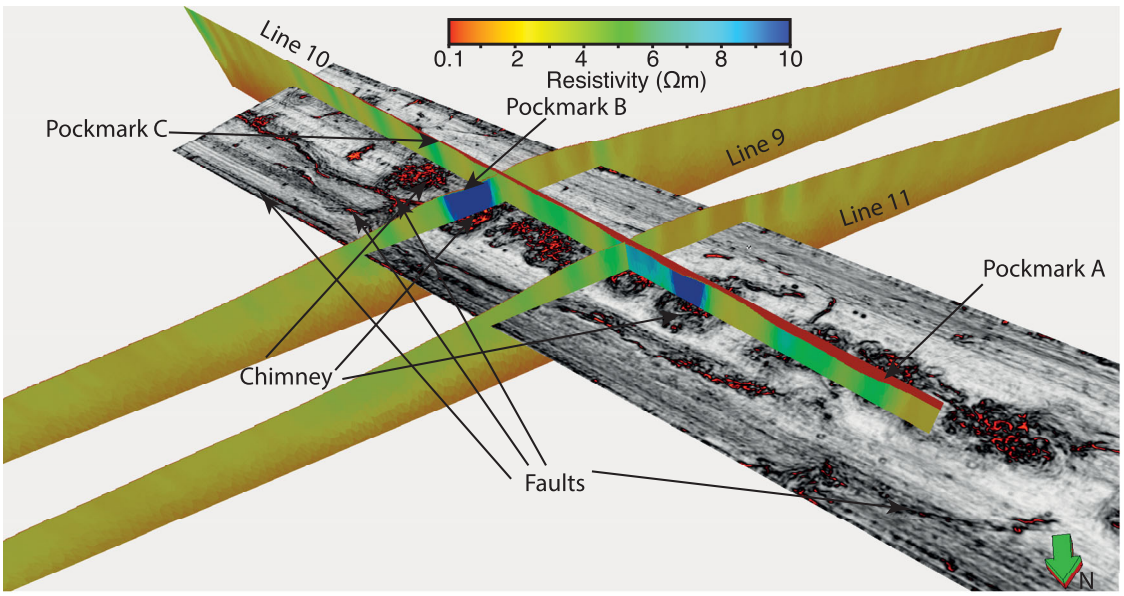

Figure 12. A time-slice of variance attribute of 3-D p-cable seismic data derived approximately 50 ms beneath the seafloor shows chaotic, incoherent structures associated with acoustic chimneys. The vertical resistivity models shown in Figures 6–8 are superimposed on the variance time-slice. The low resistivity of seawater (∼0.3 Ωm) can be seen as red on Line 10.

Gas escape chimneys are dynamic environments and understanding their internal structure and composition using remote geophysical methods is challenging. Modelling studies predict that both hydrate and free gas may coexist within these chimneys [*Liu and Flemings*, 2006, 2007; *Smith et al*., 2014b]. In the absence of velocity constraints, the reflection characteristics and variance attributes [*Bünz et al*., 2012; *Plaza-Faverola et al*., 2015] are used to interpret the composition of the chimneys along with resistivity, which is highly sensitive to fluid compositions and provide further constraints to understand these features.

In places where the CSEM lines are at the margin of a chimney the elevated resistivity is weak (Figures 11 and 2a, and 12), whereas in places where the CSEM line crosses the center of a chimney the resistivity anomaly is high (Figures 9, 10, 2a, and 12). The resistivity anomaly on Line 9 is particularly high across one of the actively seeping pockmark, whereas the resistivity anomaly across an inactive pockmark further NW on Line 10 is considerably lower (Figures 10 and 12). It is therefore difficult to infer whether the variations in resistivities beneath the pockmarks are a result of sampling differences (center or edge of chimney), or whether it is controlled by the hydrate and/or gas saturation within the chimneys.

Considerable variations in morphology and reflection characteristics are also reported within these chimneys [*Bünz et al*., 2012], which suggest differences in their internal structure and evolution [*Plaza-Faverola et al*., 2015]. Nevertheless, the evolution of most of the chimneys within the study area is thought to be partly linked to stress related faults. Periodic gas release through these chimneys [*Bünz et al*., 2012; *Panieri et al*., 2014; *Plaza-Faverola et al*., 2015] is a likely response to fault reactivation [*Plaza-Faverola et al*., 2015].

The resistivity anomaly of the active pockmark on Line 9 alone does not reveal any particular distribution of a resistive material, i.e., gas or gas hydrates in small pockets or as parts of the chimney (Figure 9b). However, the resistivity data clearly show the presence of a resistive material in the whole chimney structure. Seismic data in this chimney show several amplitude anomalies that most likely stem from either of the two aforementioned. High levels of hydrate and free gas saturations within the central chimney on Line 9 were inferred on the basis of a joint velocity and resistivity analysis presented by *Goswami et al*. [2015]. The resistivities observed within this chimney are higher than any of the other chimneys observed in our resistivity models (Figures 6–12). Coincident high-resolution SYSIF [*Ker et al*., 2010] data for Line 9 (Figure 9b) also provides further detail for the top part of the central chimney. High-amplitude chaotic reflectors and the highest resistivity within the chimney are located toward the eastern part of the chimney, suggesting higher saturations of hydrate and gas. The western part of the chimney shows slightly lower resistivities and an acoustic shadow, which might be associated with the presence of free gas. However, the asymmetry in SYSIF reflector characteristics and resistivities need to be considered carefully as the two data sets were acquired 1 year apart.

The reflection characteristics of the chimneys at the northern part of Line 10 (Figure 10) are similar to that of the chimney beneath pockmark B on Line 9. The seismic data for these chimneys image directly beneath the center of the pockmarks. The chimneys show a number of amplitude anomalies throughout their vertical extent but specifically in the upper 80–100 m. These anomalies are likely attributed to the presence of free gas and hydrates within these structures [*Bünz et al*., 2012].

The chimneys imaged beneath the edge of pockmarks are likely associated with the edges of the fluid migration pathways (Figure 12). These chimneys show elevated resistivities and occasionally upward deflecting reflectors (Figure 10), which may indicate hydrate presence at the edge of the chimneys. Hydrate lined chimneys are supported by models that study the evolution of long term chimneys [*Liu and Flemings*, 2007; *Smith et al*., 2014a] and have been previously suggested on the basis of similar features observed in 3-D reflection data from the ridge [*Bünz et al*., 2012].

The variance attribute clearly identifies faults at the ridge flanks (Figure 12), which appear as chimney features on 2-D seismic reflection data (Figure 9). The faults are supposed to play a major role in fluid flow in this area [*Plaza-Faverola et al*., 2015] and can be recognized as elongated narrow zones of discontinuity (invariance) in the 3-D seismic data (Figure 12). These faults coincide with weakly elevated resistivity anomalies indicating the presence of a resistive material in low concentrations along the fault plane. The high resistivity and localized upward dipping reflections within these features (Figure 9b) indicates likely gas hydrate presence within the faults.

Since the resistivity models are smoothed 3 times horizontally compared to the vertical direction, the focussing of high resistivities toward the center of the chimneys is likely to be a geological feature rather than an acquisition or processing footprint. This potentially indicates a relationship between gas saturation and the measured resistivity within the chimneys. Based on these observations, high free gas saturations within active chimneys can be inferred, which likely controls the gas escape through the pockmarks. Since both free gas and hydrate presence are likely within the chimney features [*Goswami et al*., 2015], the inactive chimneys and faults are more likely to contain hydrates than free gas, assuming high free gas saturation is the cause of high resistivity within the active chimneys.

5.2. Ridge Flanks

The resistivities reported outside the chimneys within the GHSZ are comparable to those of the Cascadia margin (3–5 Ωm) [*Schwalenberg et al*., 2005], offshore Norway (1–3 Ωm) [*Attias et al*., 2016], western continental slope of Svalbard (3–12 Ωm) [*Goswami et al*., 2016] and Hydrate Ridge (<5 Ωm) [*Weitemeyer et al*., 2006, 2011]. These studies focus on sediments with comparable porosities and were obtained using CSEM data.

Marine CSEM data are mainly sensitive to the transverse resistance (resistivity multiplied by thickness) [*Constable*, 2010]. Therefore, the transverse resistance of the top 180 mbsf is considered the most appropriate measure for interpretation of the resistivity models within the GHSZ. The transverse resistance of the GHSZ outside the chimneys (330–450 Ωm^2) is higher than that of the reference trend obtained from ODP Site 986 resistivity log (210 Ωm^2) (Figures 6b, 7b, and 8b), most likely due to the presence of hydrate. Small amount of free gas may also contribute to the resistivity anomaly [*Goswami et al*., 2015]. Although the seismic reflector characteristic on both flanks of the ridge appear identical on the 2-D data (Figures 9a and 11), variations between the ridge flanks can be inferred based on the joint resistivity and seismic interpretations. The transverse resistance to the east of the chimneys (400–450 Ωm^2) is slightly higher than the western flank (around 350 Ωm^2) for both Line 9 and Line 11. In addition, the variance time-slice shows a greater network of faults with a prominent continuous fault on the eastern flank of the ridge (Figure 12). These faults provide likely conduits for free gas into the GHSZ and cause higher hydrate and free gas saturations in the eastern flank, leading to higher resistivities. The high-resistivity anomalies associated with the faults extend up to the seafloor, which suggests these faults provide likely pathways for free gas throughout the strata of unconsolidated sediments at the ridge. Since the gas migration is likely to be episodic, it is not surprising that we do not see any evidence of the gas migration in seismic reflection data. The gas might also get converted to hydrate, which will be difficult to detect with the seismic reflection data.

6. Conclusion

The resistivity models obtained from Vulcan CSEM data provide useful constraints to interpret fluid escape features observed on coincident 2-D/3-D seismic reflection data at the Vestnesa Ridge. Based on the joint interpretation, the following conclusions can be made:

1. High transverse resistance within the top 180 mbsf suggests widespread presence of hydrate within the GHSZ at the Vestnesa Ridge.
2. Differences in resistivities, seismic reflector characteristics (pull-ups and push-downs), and variance attributes within the chimney structures beneath various pockmarks suggest variation in fluid composition within these features. Elevated resistivities within acoustic chimneys with seismic reflector pull-ups suggests the likelihood of higher hydrate saturation, whereas elevated resistivities with seismic reflector push-downs suggests the likelihood of gas presence within some of these fluid escape features.
3. Fluid migration at flanks likely occur through faults, where increased hydrate and free gas presence is inferred from higher resistivities.

Acknowledgments

We are grateful to the Captain, crew, and shipboard scientific party of RRS James Clark Ross cruise JCR269B for their hard work at sea. We are also thankful to Veit Huehnerbach for operating HyBIS, Laurence North, Hector Marin-Moreno, and Yee Yuan Tan for their time during DASI operation. This research would not have been possible without the funding of the National Environment Research Council (NERC), UK (grant NE/H002732/1 and NE/H022260/1). T. Minshull is supported by a Wolfson Research Merit award and S Bünz is funded by the Research Council of Norway through its Centres of Excellence funding scheme (grant 223259/F5). Seismic and CSEM data are archived at the British Oceanographic Data Centre. We would also like to thank Kerry Key for developing the MARE2DEM code and making it publicly available and David Myer for the CSEM processing codes and valuable discussions. We are also thankful to Bruno Marsset and the Ifremer's team who performed the SYSIF acquisition during JCR269A.

References

Attias, E., K. Weitemeyer, T. A. Minshull, A. I. Best, M. Sinha, M. Jegen-kulcsar, H. Sebastian, and C. Berndt (2016), Controlled-source electromagnetic and seismic delineation of sub-seafloor fluid flow structures in a gas hydrate province, offshore Norway, *Geophys. J. Int.*, *206*, 1093–1110, doi:10.1093/gji/ggw188.

Bünz, S., S. Polyanov, S. Vadakkepuliyambatta, C. Consolaro, and J. Mienert (2012), Active gas venting through hydrate-bearing sediments on the Vestnesa Ridge, offshore W-Svalbard, *Mar. Geol.*, *332-334*, 189–197, doi:10.1016/j.margeo.2012.09.012.
Collett, T. S., and J. Ladd (2000), Detection of gas hydrate with downhole logs and assessment of gas hydrate concentrations (saturations) and gas volumes on the Blake Ridge with electrical resistivity data, in *Proc. Ocean Drill. Program Sci. Results*, *164*, pp. 179–191.
Constable, S. (2010), Ten years of marine CSEM for hydrocarbon exploration, *Geophysics*, *75*(5), 75A67–75A81.
Constable, S. C., R. L. Parker, and G. Constable (1987), Occam's Inversion: A practical algorithm for generating smooth models from electromagnetic sounding data, *Geophysics*, *52*(3), 289–300.
Constable, S., P. K. Kannberg, and K. Weitemeyer (2016), Vulcan: A deep-towed CSEM receiver, *Geochem. Geophys. Geosyst.*, *17*, 1042–1064, doi:10.1002/2015GC006174.
Eiken, O., and K. Hinz (1993), Contourites in the Fram Strait, *Sediment. Geol.*, *82*(1–4), 15–32, doi:10.1016/0037-0738(93)90110-Q.
Ellis, M. H., M. C. Sinha, T. A. Minshull, J. Sothcott, and A. I. Best (2010), An anisotropic model for the electrical resistivity of two-phase geologic materials, *Geophysics*, *75*(6), E161–E170, doi:10.1190/1.3483875.
Forsberg, C. F., A. Solheim, E. Jansen, and E. S. Andersen (1999), The depositional environment of the Western Svalbard Margin during the Late Pliocene and the Pleistocene: Sedimentary facies at Site 986, *Proc. Ocean Drill. Program Sci. Results*, *162*, 233–246.
Gay, A., M. Lopez, P. Cochonat, D. Levaché, G. Sermondadaz, and M. Seranne (2006), Evidences of early to late fluid migration from an upper Miocene turbiditic channel revealed by 3D seismic coupled to geochemical sampling within seafloor pockmarks, Lower Congo Basin, *Mar. Pet. Geol.*, *23*(3), 387–399, doi:10.1016/j.marpetgeo.2006.02.004.
Goswami, B. K., K. A. Weitemeyer, T. A. Minshull, M. C. Sinha, G. K. Westbrook, A. Chabert, T. J. Henstock, and S. Ker (2015), A joint electromagnetic and seismic study of an active pockmark within the hydrate stability field at the Vestnesa Ridge, West Svalbard margin, *J. Geophys. Res.*, *120*, 6797–6822, doi:10.1002/2015JB012344.
Goswami, B., K. Weitemeyer, T. Minshull, M. Sinha, G. Westbrook, and H. Marín-Moreno (2016), Resistivity image beneath an area of active methane seeps in the continental slope of west Svalbard margin, *Geophys. J. Int.*, *207*, 1286–1302.
Hong, W. L., S. Sauer, G. Panieri, W. G. Ambrose Jr., R. H. James, A. Plaza-Faverola, and A. Schneider (2016), Removal of methane through hydrological, microbial, and geochemical processes in the shallow sediments of pockmarks along eastern Vestnesa Ridge (Svalbard), *Liminol. Oceanogr. Methods*, *61*, S324–S343, doi:10.1002/lno.10299.
Hovland, M., J. V. Gardner, and A. G. Judd (2002), The significance of pockmarks to understanding fluid flow processes and geohazards, *Geofluids*, *2*, 127–136.
Hovland, M., H. Svensen, C. F. Forsberg, H. Johansen, C. Fichler, J. H. Fosså, R. Jonsson, and H. K. Rueslåtten (2005), Complex pockmarks with carbonate-ridges off mid-Norway: Products of sediment degassing, *Mar. Geol.*, *218*(1–4), 191–206, doi:10.1016/j.margeo.2005.04.005.
Howe, J. A., T. M. Shimmield, and R. Harland (2008), Late Quaternary contourites and glaciomarine sedimentation in the Fram Strait, *Sedimentology*, *55*, 179–200, doi:10.1111/j.1365-3091.2007.00897.x.
Hustoft, S., S. Bünz, J. Mienert, and S. Chand (2009), Gas hydrate reservoir and active methane-venting province in sediments on $<$20 Ma young oceanic crust in the Fram Strait, offshore NW-Svalbard, *Earth Planet. Sci. Lett.*, *284*(1–2), 12–24, doi:10.1016/j.epsl.2009.03.038.
Jakobsson, M., et al. (2012), The International Bathymetric Chart of the Arctic Ocean (IBCAO) Version 3.0, *Geophys. Res. Lett.*, *39*, L12609, doi:10.1029/2012GL052219.
Jansen, E., M. Raymo, and P. Blum (1996), Shipboard Scientific Party 2 Hole 986A, *Proc. Ocean Drill. Program Initial Rep.*, *162*, 287–342.
Ker, S., B. Marsset, S. Garziglia, Y. L. Gonidec, D. Gibert, M. Voisset, and J. Adamy (2010), High-resolution seismic imaging in deep sea from a joint deep-towed/OBH reflection experiment: Application to a Mass Transport Complex offshore Nigeria, *Geophys. J. Int.*, *182*(3), 1524–1542.
Ker, S., Y. Le Gonidec, B. Marsset, G. K. Westbrook, D. Gibert, and T. A. Minshull (2014), Fine-scale gas distribution in marine sediments assessed from deep-towed seismic data, *Geophys. J. Int.*, *196*(3), 1466–1470, doi:10.1093/gji/ggt497.
Key, K. (2012b), Is the fast Hankel transform faster than quadrature?, *Geophysics*, *77*(3), F21–F30, doi:10.1190/geo2011-0237.1.
Key, K. (2016), MARE2DEM: A 2-D inversion code for controlled-source electromagnetic and magnetotelluric data, *Geophys. J. Int.*, *207*, 571–588.
Key, K., and J. Ovall (2011), A parallel goal-oriented adaptive finite element method for 2.5D electromagnetic modelling, *Geophys. J. Int.*, *186*(1), 137–154, doi:10.1111/j.1365-246X.2011.05025.x.
Liu, X., and P. B. Flemings (2006), Passing gas through the hydrate stability zone at southern Hydrate Ridge, offshore Oregon, *Earth Planet. Sci. Lett.*, *241*(1–2), 211–226, doi:10.1016/j.epsl.2005.10.026.
Liu, X., and P. B. Flemings (2007), Dynamic multiphase flow model of hydrate formation in marine sediments, *J. Geophys. Res.*, *112*, B03101, doi:10.1029/2005JB004227.
MacGregor, L., and J. Tomlinson (2014), Special section: Interpretation and integration of CSEM data Marine controlled-source electromagnetic methods in the hydrocarbon industry: A tutorial on method and practice, *Interpretation*, *2*(3), 13–32.
Marsset, T., B. Marsset, S. Ker, Y. Thomas, and Y. Le Gall (2010), High and very high resolution deep-towed seismic system: Performance and examples from deepwater Geohazard studies, *Deep-Sea Res., Part I*, *57*, 628–637, doi:10.1016/j.dsr.2010.01.001.
Panieri, G., R. H. James, A. Camerlenghi, V. Cesari, C. S. Cervera, I. Cacho, and G. K. Westbrook (2014), Record of methane emissions from the West Svalbard continental margin during the last 16,000 years revealed by δ13C of benthic foraminifera, *Global Planet. Change*, *122*, 151–160, doi:10.1016/j.gloplacha. 2014.08.014.
Petersen, C. J., S. Bünz, S. Hustoft, J. Mienert, and D. Klaeschen (2010), High-resolution p-cable 3D seismic imaging of gas chimney structures in gas hydrated sediments of an Arctic sediment drift, *Mar. Pet. Geol.*, *27*(9), 1981–1994, doi:10.1016/j.marpetgeo.2010.06.006.
Planke, S., F. N. Eriksen, C. Berndt, J. Mienert, and D. Masson (2009), Spotlight on technology: p-Cable high-resolution seismic, *Oceanography*, *22*, 85.
Plaza-Faverola, A., G. K. Westbrook, S. Ker, R. J. K. Exley, A. Gailler, T. A. Minshull, and K. Broto (2010), Evidence from three-dimensional seismic tomography for a substantial accumulation of gas hydrate in a fluid-escape chimney in the Nyegga pockmark field, offshore Norway, *J. Geophys. Res.*, *115*, B08104, doi:10.1029/2009JB007078.
Plaza-Faverola, A., S. Bünz, J. E. Johnson, S. Chand, J. Knies, J. Mienert, and P. Franek (2015), Role of tectonic stress in seepage evolution along the gas hydrate-charged Vestnesa Ridge, Fram Strait, *Geophys. Res. Lett.*, *42*, 733–742, doi:10.1002/2014GL062474.
Ramananjaona, C., L. MacGregor, and D. Andréis (2011), Sensitivity and inversion of marine electromagnetic data in a vertically anisotropic stratified earth, *Geophys. Prospect.*, *59*(2), 341–360, doi:10.1111/j.1365-2478.2010.00919.x.
Schwalenberg, K., E. Willoughby, R. Mir, and R. N. Edwards (2005), Marine gas hydrate electromagnetic signatures in Cascadia and their correlation with seismic blank zones, *First Break*, *23*, 57–63.
Sinha, M. C., P. D. Patel, M. J. Unsworth, T. R. E. Owen, M. R. G. Maccormack, and M. Road (1990), An active source electromagnetic sounding system for marine use, *Mar. Geophys. Res.*, *12*, 59–68.

Smith, B. D., and S. H. Ward (1974), On the computation of polarization ellipse parameters, *Geophysics*, *39*(6), 867–869.
Smith, A. J., J. Mienert, S. Bünz, and J. Greinert (2014a), Thermogenic methane injection via bubble transport into the upper Arctic Ocean from the hydrate-charged Vestnesa Ridge, Svalbard, *Geochem. Geophys. Geosyst.*, *15*, 1945–1959, doi:10.1002/2013GC005179.
Smith, A. J., P. B. Flemings, X. Liu, and K. Darnell (2014b), The evolution of methane vents that pierce the hydrate stability zone in the world's oceans, *J. Geophys. Res. Solid Earth*, *119*, 6337–6356, doi:10.1002/2013JB010686.
Sultan, N., et al. (2010), Hydrate dissolution as a potential mechanism for pockmark formation in the Niger delta, *J. Geophys. Res.*, *115*, B08101, doi:10.1029/2010JB007453.
Vogt, P. R., K. Crane, E. Sundvor, M. D. Max, and S. L. Pfirman (1994), Methane-generated (?) pockmarks on young, thickly sedimented oceanic crust in the Arctic: Vestnesa ridge, Fram strait, *Geology*, *22*, 255–258, doi:10.1130/0091-7613(1994)022<0255.
Weitemeyer, K. A., S. C. Constable, K. W. Key, and J. P. Behrens (2006), First results from a marine controlled-source electromagnetic survey to detect gas hydrates offshore Oregon, *Geophys. Res. Lett.*, *33*, L03304, doi:10.1029/2005GL024896.
Weitemeyer, K. A., S. Constable, and A. M. Tréhu (2011), A marine electromagnetic survey to detect gas hydrate at Hydrate Ridge, Oregon, *Geophys. J. Int.*, *187*(1), 45–62, doi:10.1111/j.1365-246X.2011.05105.x.
Westbrook, G. K., et al. (2009), Escape of methane gas from the seabed along the West Spitsbergen continental margin, *Geophys. Res. Lett.*, *36*, L15608, doi:10.1029/2009GL039191.